PAPER

Impacts of 5d electron binding energy and electron–phonon coupling on luminescence of Ce³⁺ in Li₆Y(BO₃)₃

Yiyi Ou, [ID] [a] Weijie Zhou, [ID] [a] Dejian Hou, [b] Mikhail G. Brik, [cde] Pieter Dorenbos, [ID] [f] Yan Huang [g] and Hongbin Liang [ID] *[a]

In this work, the crystal structure and electronic structure as well as the synchrotron radiation vacuum ultraviolet-ultraviolet-visible (VUV-UV-vis) luminescence properties of Li₆Y(BO₃)₃ (LYBO):Ce³⁺ phosphors were investigated in detail. The Rietveld refinement and DFT calculation reveal the $P2_1/c$ monoclinic crystal phase and the direct band gap of the LYBO compound, respectively. Only one kind of Ce³⁺ 4f–5d transition is resolved in terms of the low temperature VUV-UV excitation, UV-vis emission spectra and luminescence decay curves. Furthermore, by constructing the vacuum referred binding energy (VRBE) scheme and applying the frequency-degenerate vibrational model, the impacts of 5d electron binding energy and electron–phonon coupling on luminescence of Ce³⁺ in LYBO are analysed. The results show that the Ce³⁺ emission in LYBO possesses a moderate intrinsic thermal stability. With the increase in concentration, the thermal stability of the emission gets worse due to the possible thermally-activated concentration quenching. In addition, the simulation of Ce³⁺ emission profile at low temperature reveals that the 4f–5d electronic transitions of Ce³⁺ ions can be treated to couple with one frequency-degenerate vibrational mode having the effective phonon energy of ∼257 cm⁻¹ with the corresponding Huang–Rhys parameter of ∼6, which indicates a strong electron–phonon interaction of Ce³⁺ luminescence in the Li₆Y(BO₃)₃ host. Finally, the X-ray excited luminescence spectrum of the LYBO:5%Ce³⁺ phosphor is measured to check the potential scintillator applications.

1. Introduction

Due to the large absorption cross section, high efficiency, tuneable emission wavelength and fast decay of the spin- and parity-allowed 4f–5d transitions, the Ce³⁺ activated inorganic compounds have been extensively studied for their application in solid-state lighting, ionizing radiation detection, and so on.[1,2] For instance, Ce³⁺ activated Y₃Al₅O₁₂ with high quantum efficiency and good thermal stability is a commercial yellow phosphor for the white light-emitting diodes driven by a blue chip.[3] The Ce³⁺ activated LaBr₃ with large light output, excellent energy resolution, and fast decay time is a good scintillator for gamma-ray discrimination.[4] In addition, Ce³⁺ can also serve as an efficient sensitizer for other lanthanide luminescence.[5,6]

In essence, two factors impose great influence on the luminescence of Ce³⁺ in a dielectric inorganic compound. Firstly, the crystal field strength and nephelauxetic effect together determine the 5d energy (including the crystal field splitting and the centroid shift) of Ce³⁺ in a given host compound.[7] From a viewpoint of electron binding energy, the Ce³⁺ 5d electron binding energy, rather than that of 4f electron, mainly decides the absorption energy of Ce³⁺ activated phosphors.[8] Furthermore, due to the thermal ionization mechanism for Ce³⁺ emission thermal quenching, the gap of Ce³⁺ 5d electron binding energy to the bottom of host conduction band (CB) also impacts the thermal stability of Ce³⁺ luminescence.[9,10] Secondly, the electron–phonon coupling significantly influences the Ce³⁺ luminescence. The resulting Stokes shift along with the absorption wavelength of Ce³⁺ determines the emission colour of phosphors.[11] Moreover, the width of emission bands that are attributed to the vibronic transitions progressing up to several harmonics of the vibrational frequencies further affects the phosphor colour purity.[12] Consequently, it is critical to understand the influences of 5d electron binding energy and electron–phonon coupling on luminescence to develop the superior Ce³⁺ activated phosphors with desired properties.

[a] MOE Key Laboratory of Bioinorganic and Synthetic Chemistry, KLGHEI of Environment and Energy Chemistry, School of Chemistry, Sun Yat-sen University, Guangzhou 510275, China. E-mail: cesbin@mail.sysu.edu.cn

[b] School of Materials Science and Engineering, Hanshan Normal University, Chaozhou, 521041, China

[c] College of Sciences, Chongqing University of Posts and Telecommunications, Chongqing 400065, China

[d] Institute of Physics, University of Tartu, Tartu 50411, Estonia

[e] Institute of Physics, Jan Długosz University, PL-42200 Częstochowa, Poland

[f] Faculty of Applied Sciences, Delft University of Technology, Mekelweg 15, 2629 JB Delft, The Netherlands

[g] Beijing Synchrotron Radiation Facility, Institute of High Energy Physics, Chinese Academy of Sciences, Beijing 100039, China

In this work, the crystal structure and electronic structure of the host compound $Li_6Y(BO_3)_3$ (LYBO) and Ce^{3+} doped samples prepared *via* a high-temperature solid-state reaction method were investigated. The VUV-UV excitation spectra, the UV-vis emission spectra and the decay curves of doping samples at different concentrations and temperatures were studied in detail. The construction of the vacuum referred binding energy scheme[13] and the simulation with the frequency-degenerate model[14] were performed to get insight into the impacts of 5d electron binding energy and electron–phonon coupling on luminescence of Ce^{3+} in $Li_6Y(BO_3)_3$, including the intrinsic thermal stability and spectral profile of Ce^{3+} emissions. These analyses could also be applied to other Ce^{3+} doped systems and help to develop the novel phosphors with desired properties.

2. Experimental section

The Ce^{3+} doped powder samples $Li_6Y_{1-x}Ce_x(BO_3)_3$ ($x = 0.05$, 0.08, 0.10, 0.15) were synthesized *via* a conventional high-temperature solid-state reaction method. Stoichiometric amounts of starting materials Li_2CO_3 (Analytical Reagent, AR), H_3BO_3 (AR), Y_2O_3 (99.99%), and CeO_2 (99.99%) were weighted and ground finely in an agate mortar. The homogeneous mixture was calcined in an alumina crucible at 700 °C for 6 hours in thermal carbon reductive atmosphere and cooled down to room temperature (RT). Finally, the obtained products were ground into powder for further measurements. The phase purity of powder samples was checked by a Rigaku D-MAX 2200 VPC X-ray diffractometer with Cu Kα radiation ($\lambda = 1.5418$ Å) at 40 kV and 26 mA. High-quality XRD data over a 2θ range of 5° to 100° at an interval of 0.02° for Rietveld refinement was collected by a Bruker D8 advanced X-ray diffractometer with Cu Kα radiation ($\lambda = 1.5418$ Å) at 40 kV and 40 mA. The Rietveld refinement was performed by using the TOPAS-Academic program.[15] The UV-vis luminescence spectra and decay curves were recorded on an Edinburgh Instrument FLS920 combined fluorescence lifetime and steady-state spectrometer. The vacuum ultraviolet-ultraviolet (VUV-UV) excitation spectra were recorded on the beamline 4B8 of the Beijing Synchrotron Radiation Facility (BSRF).[16] The X-ray excited luminescence spectrum was recorded by using a Philips PW2253/20 X-ray tube and a Cu anode operating at 40 kV and 25 mA at Delft University of Technology, the Netherlands.

The atomic structures of the LYBO host unit cell were fully relaxed by using periodic density functional theory (DFT) calculations with the PBE functional[17] as well as the PBE0 hybrid functional,[18] as implemented in the VASP code.[19,20] The electrons of $Li(1s^2 2s^1)$, $Y(4s^2 4p^6 4d^1 5s^2)$, $B(2s^2 2p^1)$, and $O(2s^2 2p^4)$ were treated as valence electrons, and their interactions with the respective cores were described by the projected augmented wave (PAW) method.[21] The convergence criteria for total energies and atomic forces were set to 10^{-6} eV and 0.01 eV Å^{-1}, respectively. A $3 \times 2 \times 3$ k-point grid in the Monkhorst–Pack scheme was used to sample the Brillouin zone, with a cutoff energy of 530 eV for the plane wave basis.

3. Results and discussion

3.1 Crystal structure and electronic structure of LYBO

Rietveld refinement of high-quality XRD data of synthesized LYBO compound was conducted by using $P2_1/c$ (monoclinic) structure as an initial model (Fig. 1a).[22] The reliability factors R_{wp} (~4.983%), R_p (~3.319%) and R_B (~2.876%) all imply a good fitting quality. No other impurity was found, indicating the single pure phase of the synthesized sample. The refined structural parameters are listed in Table 1. The compound LYBO has a monoclinic structure with space group $P2_1/c$ and the lattice parameters are $a = 7.180$ (1) Å, $b = 16.43$ (2) Å, $c = 6.634$ (1) Å, $\beta = 105.3$ (1) deg, $V = 754.9$ Å^3 and $Z = 4$. All the constituent ions sit on the 4e Wyckoff positions. There are six kinds of lithium ions: four of them coordinate to five oxygens to construct the distorted Li–O trigonal bipyramids, and two remaining link to four oxygens to form the Li–O tetrahedron. Three kinds of boron ions all coordinate to three oxygens to form the planar triangles. There is only one type of Y^{3+} ion and it is surrounded by eight oxygens with C_1 point symmetry, which forms a Y–O distorted tetragonal prism. The average Y–O bond length is ~2.376 Å. The distance between the nearest Y^{3+} ions is ~3.879 Å. As shown in the inset of Fig. 1a, these Li–O, Y–O polyhedral and B–O planar triangles share their apexes or edges to construct the structural framework of LYBO compound.

The atomic structures of LYBO unit cell were optimized, and the calculated parameters with the PBE (PBE0) functional are $a = 7.237$ (7.176) Å, $b = 16.501$ (16.332) Å, $c = 6.711$ (6.641) Å, $\beta = 105.488$ (105.428) deg, in good agreement with experimental data. The band structure of LYBO calculated with the PBE functional is displayed in Fig. 1b, showing a direct band gap of 4.83 eV with the valence band maximum (VBM) and the conduction band minimum (CBM) both located at the k-point Γ. It is well known that the band gaps of inorganic compounds are usually underestimated by DFT-PBE calculations, and can be obtained quite accurately by hybrid DFT calculations. Fig. 1c gives the calculated total and orbital projected densities of states (DOS) for LYBO with the PBE0 functional. The band gap is predicted to be 7.26 eV, close to the experimentally estimated value of 7.44 eV as discussed below. The top of the valence band is dominated by O 2p states, and the bottom of the conduction band is mainly composed of Y 4d states with small contributions from O 2s, 2p states. The conduction band edge is constituted by a small peak at 7.26 eV above the VBM, which is mainly derived from s-character states of O atoms. It is noted that, with the PBE functional, the calculated orbital characters for the valence and conduction bands are basically the same, although with a much smaller band gap.

For the Ce^{3+} doped samples, their structures were studied *via* XRD technique. Fig. 1d shows the representative result. The pattern of concentrated sample $Li_6Y_{0.85}Ce_{0.15}(BO_3)_3$ (LYBO:15% Ce^{3+}) agrees well with the refined result, which implies a single LYBO phase. Due to the comparable effective ionic radii [$r(Y^{3+})$ = 101.9 pm, $r(Ce^{3+})$ = 114.3 pm][23] and the same valence state (3+), the doped Ce^{3+} ions are thought to enter Y^{3+} sites in LYBO.
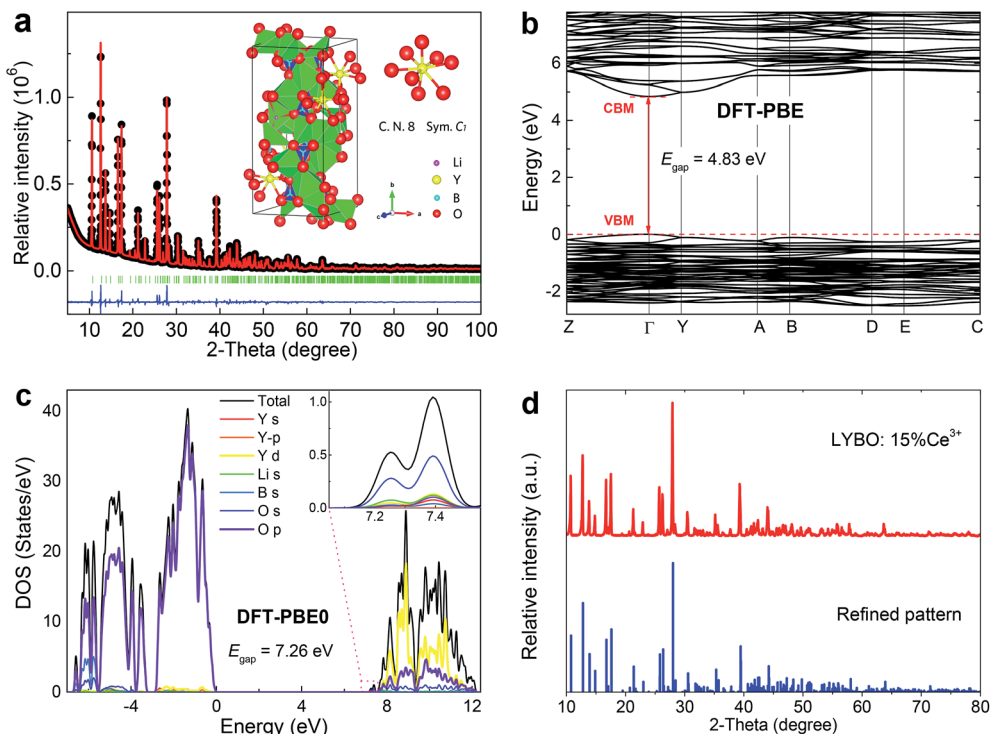
Fig. 1 (a) Rietveld refinement of high-quality XRD data of synthesized LYBO compound at RT. The black-dot line represents the experimental result, the red line is the fitting curve, the green bars show the Bragg positions, and the blue line is the difference between experimental and fitting result. The inset shows the structural diagram of LYBO and the coordinate environment of Y^{3+} ion. (b) The band structure of LYBO calculated with the DFT-PBE method. (c) Total and orbital-projected DOSs for LYBO obtained with the DFT-PBE0 method. The Fermi level is set at zero energy. (d) XRD pattern of concentrated sample $Li_6Y_{0.85}Ce_{0.15}(BO_3)_3$ (LYBO:15%Ce^{3+}) at RT.

Table 1 Refined structural parameters of compound LYBO at RT

Atom	Site	x	y	z	occ.	beq
Y1	4e	0.0801 (3)	0.3112 (1)	0.1542 (3)	1	1.12
Li1	4e	0.0713 (2)	0.5040 (2)	0.1735 (5)	1	1.28
Li2	4e	0.550 (1)	0.4696 (9)	0.675 (2)	1	1.28
Li3	4e	0.712 (2)	0.2050 (8)	0.867 (2)	1	1.28
Li4	4e	0.306 (2)	0.4639 (9)	0.941 (2)	1	1.28
Li5	4e	0.438 (2)	0.2945 (9)	0.952 (2)	1	1.28
Li6	4e	0.862 (2)	0.0519 (8)	0.917 (2)	1	1.28
B1	4e	0.440 (1)	0.3852 (6)	0.312 (1)	1	1.15
B2	4e	0.715 (1)	0.1201 (5)	0.497 (1)	1	1.15
B3	4e	0.083 (1)	0.1356 (5)	0.161 (1)	1	1.15
O1	4e	0.6078 (8)	0.4211 (3)	0.4242 (8)	1	1.39
O2	4e	0.4206 (8)	0.3022 (3)	0.2738 (8)	1	1.39
O3	4e	0.2782 (8)	0.0685 (3)	0.7298 (8)	1	1.39
O4	4e	0.5361 (8)	0.0887 (3)	0.4133 (8)	1	1.39
O5	4e	0.7400 (8)	0.2970 (3)	0.0556 (8)	1	1.39
O6	4e	0.8773 (8)	0.0745 (3)	0.5400 (8)	1	1.39
O7	4e	0.0873 (8)	0.0528 (3)	0.1769 (8)	1	1.39
O8	4e	0.1472 (8)	0.1847 (3)	0.3338 (7)	1	1.39
O9	4e	0.0087 (8)	0.3263 (3)	0.4735 (8)	1	1.39

3.2 Photoluminescence and VRBE scheme of Ce^{3+} in LYBO

Fig. 2a shows the VUV-UV excitation (λ_{em} = 410 nm) spectra of sample $Li_6Y_{0.95}Ce_{0.05}(BO_3)_3$ (LYBO:5%Ce^{3+}) recorded by using the xenon lamp (curve 1) and synchrotron light (curve 2) at 77 and 30 K, respectively. These two curves display a good

consistence in their energetic overlapping range of 3.93–4.07 eV, *viz.*, 304–315 nm. The excitation band at ∼7.04 eV can be assigned as the host exciton creation absorption of LYBO.[24] Thus, the corresponding exciton creation energy (E_{ex}) is ∼7.04 eV. By adopting a value of $0.008 \times (E_{ex})^2$ for the exciton binding energy,[25] the bottom of CB is estimated to be about 7.04 + 0.40 = 7.44 eV higher than the top of VB. This mobility band gap value is near that of $LiCaBO_3$ (∼7.78 eV),[26] $Ca_3La_3(BO_3)_5$ (∼7.65 eV),[27] and $Ba_2Ca(BO_3)_2$ (∼7.61 eV).[28] In addition, the other low-lying excitation bands in Fig. 2a can be aligned to the 5d excitation bands of Ce^{3+} in LYBO. Since the Ce^{3+} ion enters the eight-fold coordinated Y^{3+} sites with C_1 point symmetry, the $5d_1$ configuration of Ce^{3+} should be split into five levels by crystal field. In the related literature,[24] due to the severe over-lapping of Ce^{3+} 5d excitation bands in LYBO, only four bands at ∼345 nm (∼3.59 eV), ∼305 nm (∼4.06 eV), ∼240 nm (∼5.16 eV), and ∼217 nm (∼5.71 eV) are well resolved at RT and one high-lying excitation band remains vague. In our case, the band I at ∼3.57 eV (∼347 nm) in curve 1 can be assigned to the lowest 5d excitation ($4f–5d_1$) band. To further determine the energies of higher 5d excitation bands of Ce^{3+} and host absorption, we fitted the curve 2 by using a sum of five Gaussian functions. As shown in the inset of Fig. 2a, the band VI at ∼7.04 eV corresponds to the host exciton creation absorption of LYBO as discussed above; the bands II (∼4.04 eV), III (∼5.16 eV) and IV (∼5.91 eV) are in good accordance with the above-cited reference; the band V at ∼6.39 eV is then tentatively assigned to the

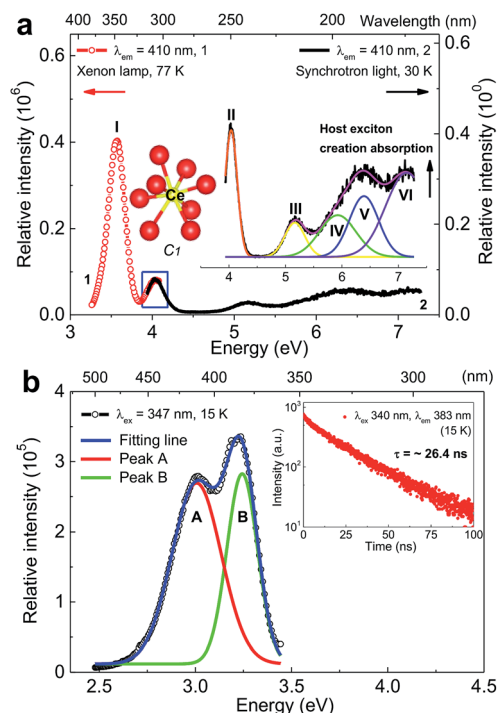**Fig. 2** (a) VUV-UV excitation (λ_{em} = 410 nm) spectra of sample Li$_6$-Y$_{0.95}$Ce$_{0.05}$(BO$_3$)$_3$ (LYBO:5%Ce^{3+}) collected by the xenon lamp (curve 1) and synchrotron light (curve 2) at 77 and 30 K, respectively. The insets show the coordination environment of Ce^{3+} and the related Gaussian fitting results of curve 2. (b) Emission (λ_{ex} = 347 nm) spectrum of sample LYBO:5%Ce^{3+} at 15 K and the related Gaussian fitting results. The inset shows the luminescence decay curve (λ_{ex} = 340 nm, λ_{em} = 383 nm) of Ce^{3+} emission at 15 K.

highest 5d excitation band of Ce^{3+}. With these assignments, the centroid energy of Ce^{3+} 5d states in LYBO, *i.e.* the arithmetic mean value of five Ce^{3+} 5d excitation energies, is calculated to be ~5.01 eV. Compared to the free Ce^{3+} ion case (~6.35 eV), the centroid shift energy (ε_c) is ~1.34 eV for our case, which is similar to other borates such as LuBO$_3$ (~1.39 eV),[29] Sr$_2$-Mg(BO$_3$)$_2$ (~1.36 eV)[30] and Ba$_2$Mg(BO$_3$)$_2$ (~1.34 eV).[31] This indicates that these host compounds have similar covalence, spectroscopic polarizability and nephelauxetic effect.[29] In addition, the crystal field splitting energy (E_{cfs}) of Ce^{3+} 5d states in LYBO, *i.e.* the energy difference between the highest and lowest 5d excitation bands of Ce^{3+}, is estimated to be ~2.82 eV. Compared to the E_{cfs} values of other Ce^{3+} ions occupying the sites with similar coordination number (8) and point symmetry (C$_1$) in borates like YBO$_3$ (~2.72 eV),[32] Ca$_3$(BO$_3$)$_2$ (~2.34 eV)[24] and SrB$_2$O$_4$ (~2.16 eV),[33] the E_{cfs} value of our case is a bit larger, implying its greater distortion of coordination polyhedron and smaller site size.[34]

Fig. 2b shows the emission (λ_{ex} = 347 nm) spectrum of sample LYBO:5%Ce^{3+} at 15 K. A sum of two Gaussian functions was applied to fit this curve. Two fitting emission bands (A and B) are at ~3.01 eV (~412 nm) and ~3.24 eV (~383 nm), respectively. They pertain to the transitions from the lowest 5d excited state (5d$_1$) to the 4f ground states ^{2}F$_{7/2}$ and ^{2}F$_{5/2}$ of Ce^{3+}, respectively. Their energy difference is about 0.23 eV, which is near the common value (0.25 eV).[35] The Stokes shift of Ce^{3+} in LYBO is

calculated to be ~0.33 eV by using the peak energies of 4f-5d$_1$ excitation band I and emission band B. It is quite normal for Ce^{3+} luminescence.[36] The luminescence decay curve (λ_{ex} = 340 nm, λ_{em} = 383 nm) at 15 K in the inset of Fig. 2b slightly deviates from the single exponential behaviour, which indicates a small concentration quenching of Ce^{3+} emission. Then, the lifetime of Ce^{3+} emission is fitted to be ~26.4 ns, which is close to the average result (~29 ns) of Li$_6$(Y,Lu)(BO$_3$)$_3$ mixed crystals in reference.[37]

As a useful tool to evaluate the binding energies of lanthanides, especially the Ce^{3+} ions, in host compounds and study their impacts on the lanthanide luminescence, the vacuum referred binding energy (VRBE) scheme of lanthanide 4f and 5d states in LYBO is then constructed in Fig. 3. The required experimental data include the mobility host band gap E_{BG} (~7.44 eV, see arrow 1 in Fig. 3) of LYBO, the lowest 5d excitation energy (E_{5d_1}) of Ce^{3+} (~3.57 eV, see arrow 2) in LYBO, the centroid shift energy (ε_c) of Ce^{3+} 5d states (~1.34 eV), and the O^{2-} → Eu^{3+} charge transfer energy E_{CT} (~4.96 eV, see arrow 3).[38] The related semi-empirical models and construction process[39] are briefly introduced below.

Firstly, due to their similar fashion affected by the chemical environment, the Coulomb repulsion energy U(6, LYBO) representing the difference between the 4f ground state binding energies of Eu^{2+} and Eu^{3+} in LYBO, is estimated to be ~6.98 eV by using the ε_c of Ce^{3+} 5d states as shown in eqn (1).[32] This obtained value falls in a common range of 6–7.6 eV for U(6, A) in inorganic host A.[32] Then, based on the chemical shift model which employs a simple Coulomb repulsion interaction between 4f electrons and a hypothetic environment screening charge to describe the rises of Eu^{2+}/Eu^{3+} 4f electron binding energies,[8] the VRBE of Eu^{2+} 4f ground state (g. s.) E_{4f}(Eu^{2+}) is calculated to be about −4.06 eV with eqn (2). Consequently, the binding energy of Eu^{3+} 4f ground state E_{4f}(Eu^{3+}) = E_{4f}(Eu^{2+}) − U(6, LYBO) = −4.06 − 6.98 = −11.04 eV relative to the vacuum level. With these two 4f ground state VRBEs of Eu^{2+}/Eu^{3+} ions as the pinpoints, the 4f ground state VRBEs of other divalent and trivalent lanthanide ions (Ln^{2+}/Ln^{3+}) can be derived in LYBO by using the corresponding universal shapes of zigzag curves for Ln^{2+}/Ln^{3+}.[32] Therefore, the VRBE of Ce^{3+} 4f ground state E_{4f}(Ce^{3+}) is calculated to be about −5.80 eV. By adding the Ce^{3+} lowest 5d excitation energy (E_{5d_1}, ~3.57 eV), the VRBE of Ce^{3+} lowest 5d excited state is around −2.23 eV.
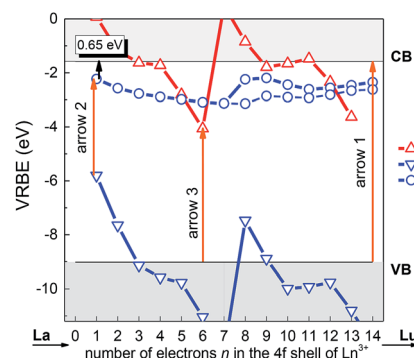

Fig. 3 Vacuum referred binding energy (VRBE) diagram of lanthanide ions in LYBO.

$$U(6, \text{LYBO}) = 5.44 + 2.834e^{-\varepsilon_c/2.2} \text{ (eV)} \qquad (1)$$

$$E_{4f}(\text{Eu}^{2+}) = -24.92 + \frac{18.05 - U(6, \text{LYBO})}{0.777 - 0.0353U(6, \text{LYBO})} \text{ (eV)} \qquad (2)$$

In addition, the charge transfer model[40] demonstrates that the $O^{2-} \rightarrow Eu^{3+}$ charge transfer energy provides the 4f ground state binding energy of Eu^{2+} relative to the top of valence band that is comprised by O 2p orbitals. Thus, the VRBE of electrons in the top of valence band is $E_{4f}(Eu^{2+}) - E_{CT} = -4.06 - 4.96 = -9.02$ eV and that of electrons in the bottom of conduction band is $-9.02 + E_{BG} = -1.58$ eV.

Generally, the intrinsic thermal quenching of Ce^{3+} f–d emission is thought to be mainly caused by the thermal ionization of electrons from the lowest 5d excited state to the bottom of CB in the isolated Ce^{3+} scenario where not taking the effect of concentration quenching into account.[41] Therefore, when the binding energy of Ce^{3+} lowest 5d state is known, its energy gap to the bottom of conduction band can be a clue that evaluates the thermal stability of Ce^{3+} f–d emission. From the constructed VRBE scheme of lanthanide ions in LYBO (Fig. 3), one can immediately obtain this energy gap is about 0.65 eV, which is smaller when compared to those of Ce^{3+} in other hosts, such as LiCaBO$_3$ ($\sim$0.74 eV),[26] KSrPO$_4$ ($\sim$1.27 eV),[42] and so on. This implies that the Ce^{3+} emission in LYBO host may possess a moderate thermal stability. When the doping concentration increases, the thermal stability of Ce^{3+} f–d emission is further influenced by the thermally-activated concentration quenching.[43] We will discuss it later.

The influence of doping concentration on Ce^{3+} emission is investigated as follows. Fig. 4 displays the highest-height-normalized emission ($\lambda_{ex} = 347$ nm) spectra of samples LYBO:xCe^{3+} ($x = 0.05$–0.15) at RT. Their spectral profiles and energetic positions almost keep unchanged. Only the relative intensity of emission band at high-energetic side (375–400 nm) slightly decreases with the doping concentration increasing, which is caused by the enhanced self-absorption of Ce^{3+} emissions. The inset of Fig. 4 shows that the integrated emission intensity of Ce^{3+} firstly increases in the concentration range of 0.05–0.10, and then it drops at $x = 0.15$. Consequently, the concentration quenching occurs in this concentration range,

viz., the excitation energy is more possibly transferred to the traps or quenching sites via energy migration between Ce^{3+} ions rather than emitted radiatively.[35]

In addition, the thermal stability of Ce^{3+} emission is studied. It is believed that the temperature-dependent luminescence decay curves of Ce^{3+} emissions give the more precise information on their thermal quenching properties compared to the intensity measurements.[43] Consequently, the luminescence decay curves ($\lambda_{ex} = 340$ nm, $\lambda_{em} = 383$ nm) of samples LYBO:xCe^{3+} ($x = 0.05$–0.10) in the temperature range of 15–450 K are collected as shown in Fig. 5a–c. With the increase of temperature, the Ce^{3+} luminescence decay turns faster, which indicates that the thermal quenching of Ce^{3+} emission happens. More clearly, we further extracted the lifetime values of Ce^{3+} emissions in Fig. 5d via the average lifetime equation.[44] For the results of sample LYBO:5%Ce^{3+}, there are two stages separated by about 300 K: (i) when the temperature is lower than 300 K, the lifetime values seem unchanged ($\sim$26.1 ns) and the platform implies no thermal quenching in this temperature range; (ii) when the temperature exceeds 300 K, the lifetime values gradually decrease due to the thermal quenching of Ce^{3+} emission. As for other concentrated samples, the temperature points corresponding to the beginning of the thermal quenching are about 250 and 200 K for samples LYBO:8%Ce^{3+} and LYBO:10%Ce^{3+}, respectively, which indicate that the Ce^{3+} emissions turn to thermally quench more easily when the doping concentration increases. We then used the Arrhenius equation[45] to fit the lifetime data in Fig. 5d and the obtained activation energy (E_a) values are $\sim$0.24, $\sim$0.19, and $\sim$0.15 eV for these three samples, which further confirm the worse thermal stability of Ce^{3+} emissions in the concentrated samples. In fact, these phenomena are because of the thermally-activated concentration quenching of Ce^{3+} emissions at high-doping level.[43] From the decreasing lifetime values ($\sim$26.1, $\sim$25.4, and $\sim$23.9 ns) corresponding to the thermally-stable platforms of samples LYBO:xCe^{3+} ($x = 0.05$–0.10) in Fig. 5d, it is evident that the Ce^{3+} emissions experience the concentration quenching in this investigated range, which is consistent with the results in Fig. 4. Consequently, when the temperature increases, the energy transfer between Ce^{3+} ions may be thermally enhanced and finally leads to the result that the excitation energy is more possibly transferred to the traps or quenching sites, i.e. the more severe concentration quenching. As for the difference between the VRBE-scheme-derived energy gap and the Arrhenius-equation-fitted activation energies that both describe the thermal quenching properties of Ce^{3+} emission, it can be related to the lattice relaxation process.[45]

3.3 Electron–phonon coupling of Ce^{3+} in LYBO

To further study the impact of electron–phonon coupling on Ce^{3+} luminescence in LYBO host, we select the emission ($\lambda_{ex} = 347$ nm) spectrum of sample LYBO:5%Ce^{3+} at 15 K as shown in Fig. 6 as a presentation. Generally, at low temperature, the vibronic emission transitions of Ce^{3+} ions are thought to occur from the zero-phonon level ($N = 0$) of the initial state (5d$_1$ state). The probability (p_N) for a transition from the zero-phonon level
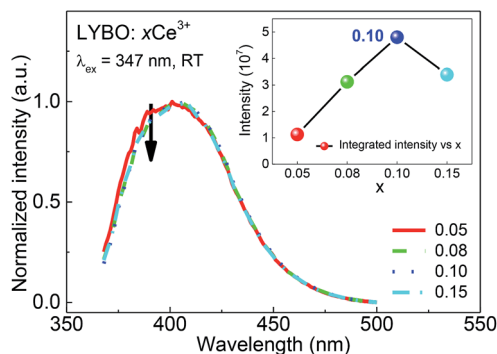

Fig. 4 Highest-height-normalized emission ($\lambda_{ex} = 347$ nm) spectra of sample LYBO:xCe^{3+} ($x = 0.05$–0.15) at RT. The inset shows the integrated emission intensity as a function of doping concentration.
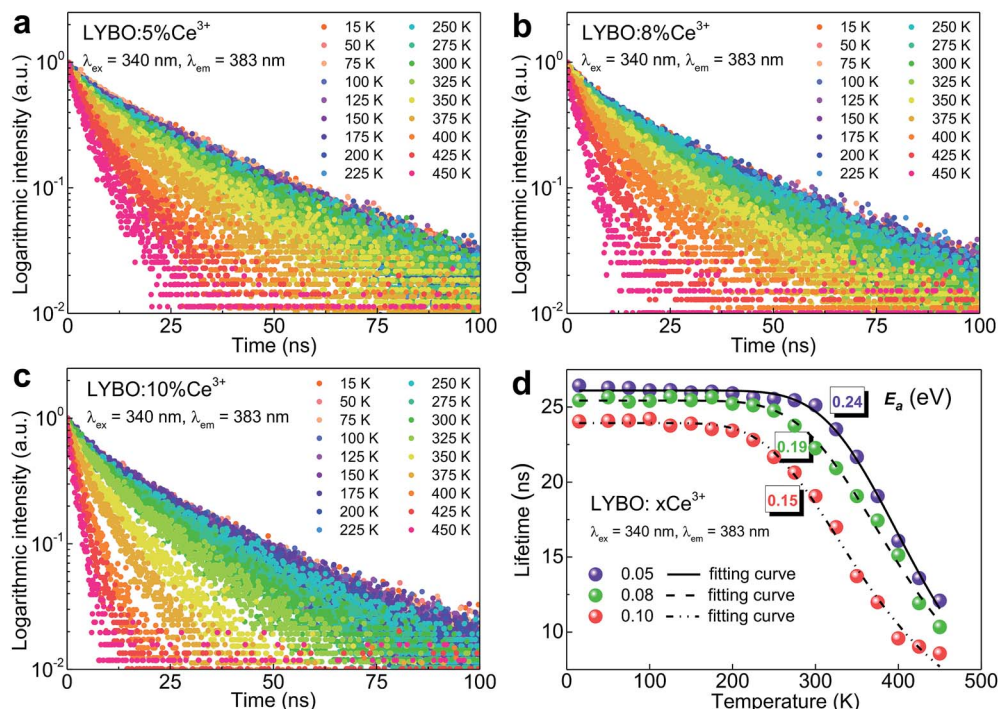
Fig. 5 (a–c) Luminescence decay curves ($\lambda_{ex} = 340$ nm, $\lambda_{em} = 383$ nm) of samples LYBO:xCe^{3+} ($x = 0.05$–0.10) in the temperature range of 15–450 K. (d) Temperature-dependent lifetime values of Ce^{3+} emissions and corresponding fitting results.

of 5d$_1$ state to the Nth vibrational level ($N\hbar\omega$) of the final state, such as 4f^1 ^{2}F$_{5/2}$ or ^{2}F$_{5/2}$ state, can be expressed in the framework of Franck–Condon principle as follows:[46]

$$p_N = \frac{e^{-S} S^N}{N!} \quad (3)$$

where S is the Huang–Rhys parameter. To simulate the vibronic spectrum, a Gaussian shaped band is superimposed on each vibronic transition line, and the resultant spectral intensity function is[14]

$$f_N(E) = \frac{e^{-S} S^N}{N!} \frac{1}{\sqrt{2\pi N\sigma^2}} \exp\left[-\frac{(E - E_0 + N\hbar\omega)^2}{2N\sigma^2}\right] \quad (4)$$

where E_0 is the transition energy of the zero-phonon line, $\hbar\omega$ is the phonon energy, and σ characterizes the bandwidth. For Ce^{3+} in LYBO, the emission spectrum can be approximately considered as a superimposition of two vibronic spectra associated with the electronic transitions 5d$_1$ → ^{2}F$_{5/2}$, ^{2}F$_{7/2}$. Moreover, instead of taking into account of all vibrational modes involved in the vibronic transitions without detailed information on the vibrational frequencies and coupling strength, a feasible approach would be to use a degenerate mode with the characteristic frequency and linewidth to effectively account for their contributions.[14,47] Based on these approximations, the spectral profile function for Ce^{3+} emission at low temperature may be expressed as

$$I(E) = \sum_k I_k \sum_{N=0} \frac{e^{-S} S^N}{N!} \frac{\exp\left[\frac{-(E - E_{0\_k} + N\hbar\omega)^2}{2(\sigma_0^2 + N\sigma_1^2)}\right]}{\sqrt{2\pi(\sigma_0^2 + N\sigma_1^2)}} \quad (5)$$

where I_k and E_{0-k} ($k = 1, 2$) represent the intensities and zero-phonon-line energies of 5d$_1$ → ^{2}F$_{5/2}$, ^{2}F$_{7/2}$ transitions, respectively, σ_0, and σ_1 characterize the linewidths for the zero-phonon and vibronic lines, respectively, and the summation over N is up to $N = 10$. With this expression, we simulated the Ce^{3+} emission spectrum by using the MAPLE code, and the result is displayed in Fig. 6. It shows a good agreement between simulated and experimental emission spectra, and the small disparity at the tail of the curve may be due to the existence of some Ce^{3+} distorted sites.[26] Table 2 lists the optimized value for the fitting parameters. One sees that the characteristic vibrational energy ($\hbar\omega$) of the degenerate vibrational mode is 257 cm^{-1}, which falls in the lower energy range of the Raman spectrum of Li$_6$Y(BO$_3$)$_3$.[48] The optimized Huang–Rhys parameter S is ~6, which indicates a strong electron–phonon
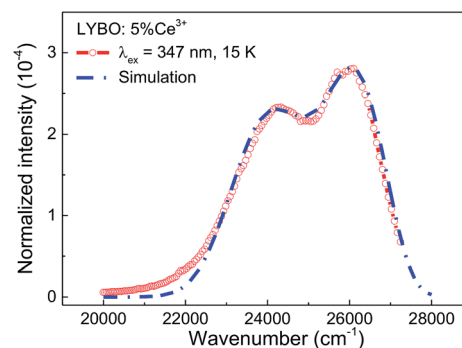

Fig. 6 Normalized emission ($\lambda_{ex} = 347$ nm) spectrum of sample LYBO:5%Ce^{3+} at 15 K and the simulated curve via the frequency-degenerate model.

Table 2 Intensity constant ratios, zero-phonon line energies (E), vibrational energy ($\hbar\omega$), Huang–Rhys parameter (S), and linewidth (σ) values obtained from the simulation process

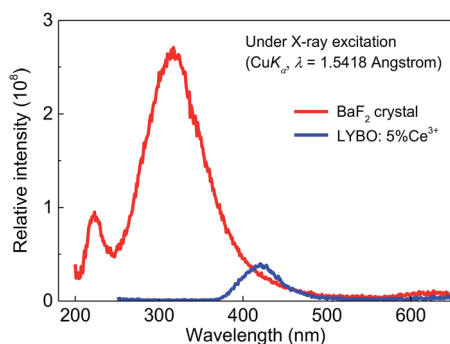| k	I_k/I_1	E_{0_k} (cm^{-1})	$\hbar\omega$ (cm^{-1})	S	σ_0, σ_1 (cm^{-1})
1	1	27 500	257	6	100, 220
2	0.85	26 600			

Fig. 7 X-ray excited luminescence (XEL) spectra of sample LYBO:5% Ce^{3+} and BaF$_2$ crystal at RT.

interaction of Ce^{3+} luminescence in Li$_6$Y(BO$_3$)$_3$. This result is also consistent with the large stokes shift ($\sim$2661 cm^{-1}) of Ce^{3+} luminescence as discussed above, and the observation that there are no obvious zero-phonon lines in the excitation and emission spectra.

3.4 X-ray excited luminescence of Ce^{3+} in LYBO

Finally, the X-ray excited luminescence measurement is carried out to check the potential scintillator application of sample LYBO:5%Ce^{3+}. The X-ray with a wavelength of 1.5418 Å is used as the excitation source. Fig. 7 displays the X-ray excited luminescence spectra of sample LYBO:5%Ce^{3+} at RT. Its spectral profile and energetic position are similar to that under UV excitation in Fig. 4. To further estimate its scintillation light yield, the BaF$_2$ crystal is also measured at the same condition as shown in Fig. 7. By calculating the ratio of the integrated intensity of sample LYBO:5%Ce^{3+} with that of BaF$_2$ ($\sim$8880 ph MeV^{-1}) crystal, its scintillation light yield is then estimated to be $\sim$864 ph MeV^{-1}, which indicates that the sample LYBO:5% Ce^{3+} is not suitable for X-ray detection scintillators.

4. Conclusions

In summary, we have systematically studied the crystal structure, the electronic structure and the synchrotron radiation VUV-UV excitation, the UV-vis emission spectra and the luminescence decay dynamics of LYBO:Ce^{3+} phosphors at different concentrations and temperatures. The pure $P2_1/c$ monoclinic single phase of synthesized samples is confirmed by the Rietveld refinement. The DFT calculations reveal that the LYBO host has a direct band gap. The top of VB mainly comprises of the 2p orbitals of O atoms, while the bottom of CB is mostly made up

of the 4d orbitals of Y atoms. The calculated band gap of LYBO is $\sim$7.26 eV, which is close to the experimental result ($\sim$7.44 eV). The low temperature VUV-UV excitation spectrum of sample LYBO:5%Ce^{3+} gives the energies of five crystal-field-splitting 5d states of Ce^{3+} ions at only one kind of Y^{3+} sites as $\sim$3.57, $\sim$4.04, $\sim$5.16, $\sim$5.91, $\sim$6.39 eV, respectively. Consequently, the centroid energy of Ce^{3+} 5d states in LYBO is $\sim$5.01 eV and the corresponding crystal field splitting energy is $\sim$2.82 eV. Furthermore, by constructing the VRBE scheme of lanthanides in LYBO host, the binding energy of Ce^{3+} lowest 5d electron is evaluated to be $\sim$−2.23 eV and this value shows an energy gap ($\sim$0.65 eV) to the bottom of the host CB, which indicates that the Ce^{3+} emission in LYBO may possess a moderate intrinsic thermal stability. However, the more concentrated samples are found to have worse thermal stability due to the possible thermally-activated concentration quenching. In addition, to study the impact of electron–phonon coupling on Ce^{3+} luminescence in LYBO host, the low temperature emission spectrum of sample LYBO:5%Ce^{3+} is simulated by using one frequency-degenerate vibrational mode. The results show that the zero-phonon lines of the 5d$_1$ → ^{2}F$_{5/2}$, ^{2}F$_{7/2}$ transitions are located at $\sim$27 500 and $\sim$26 600 cm^{-1}, respectively. The degenerate mode has an effective phonon energy of $\sim$257 cm^{-1}. The obtained Huang–Rhys parameter is $\sim$6, which indicates a strong electron–phonon interaction of Ce^{3+} luminescence in Li$_6$Y(BO$_3$)$_3$. The X-ray excited luminescence spectrum shows that sample LYBO:5%Ce^{3+} is not suitable to serve as X-ray detection scintillators. These results provide an understanding of the impacts of 5d electron binding energy and electron–phonon coupling on luminescence of Ce^{3+} in LYBO, which can be also applied to other Ce^{3+} doped systems and help to develop the novel phosphors with desired properties.

Conflicts of interest

There are no conflicts to declare.

Acknowledgements

References

1 Z. G. Xia and A. Meijerink, *Chem. Soc. Rev.*, 2017, **46**, 275–299.

2 P. A. Tanner, L. Zhou, C. K. Duan and K.-L. Wong, *Chem. Soc. Rev.*, 2018, **47**, 5234–5265.

3 L. X. Ning, X. W. Ji, Y. Y. Dong, W. Jin, Y. C. Huang, Z. F. Pan and P. A. Tanner, *J. Mater. Chem. C*, 2016, **4**, 5214–5221.

4 E. V. D. van Loef, P. Dorenbos and C. W. E. van Eijk, *Appl. Phys. Lett.*, 2001, **79**, 1573–1575.

5 J. S. Huo, L. P. Dong, W. Lü, B. P. Shao and H. P. You, *Phys. Chem. Chem. Phys.*, 2017, **19**, 17314–17323.

6 C. Y. Xu, H. X. Guan, Y. H. Song, Z. C. An, X. T. Zhang, X. Q. Zhou, Z. Shi, Y. Sheng and H. F. Zou, *Phys. Chem. Chem. Phys.*, 2018, **20**, 1591–1607.

7 L. X. Ning, L. H. Lin, L. L. Li, C. B. Wu, C.-K. Duan, Y. F. Zhang and L. Seijo, *J. Mater. Chem.*, 2012, **22**, 13723–13731.

8 P. Dorenbos, *Phys. Rev. B: Condens. Matter Mater. Phys.*, 2012, **85**, 165107.

9 D. J. Hou, W. J. Zhou, C. Wu, P. Dorenbos, H. B. Liang, T.-K. Sham, B. B. Zhang, Y. Huang and Y. Tao, *Phys. Chem. Chem. Phys.*, 2015, **17**, 22035–22041.

10 Y. Y. Ou, W. J. Zhou, C. M. Liu, L. T. Lin, M. G. Brik, P. Dorenbos, Y. Tao and H. B. Liang, *J. Phys. Chem. C*, 2018, **122**, 2959–2967.

11 Q. Peng, C. M. Liu, D. J. Hou, W. J. Zhou, C.-G. Ma, G. K. Liu, M. G. Brik, Y. Tao and H. B. Liang, *J. Phys. Chem. C*, 2016, **120**, 569–580.

12 D. Y. Zhai, L. X. Ning, Y. C. Huang and G. K. Liu, *J. Phys. Chem. C*, 2014, **118**, 16051–16059.

13 H. D. Luo, A. J. J. Bos, A. Dobrowolska and P. Dorenbos, *Phys. Chem. Chem. Phys.*, 2015, **17**, 15419–15427.

14 G. K. Liu, *J. Lumin.*, 2014, **152**, 7–10.

15 A. A. Coelho, *Coelho Software, Version 4, Topas Academic*, Brisbane, Australia, 2005.

16 Y. Tao, Y. Huang, Z. H. Gao, H. Zhuang, A. Y. Zhou, Y. L. Tan, D. W. Li and S. S. Sun, *J. Synchrotron Radiat.*, 2009, **16**, 857–863.

17 J. P. Perdew, K. Burke and M. Ernzerhof, *Phys. Rev. Lett.*, 1996, **77**, 3865–3868.

18 J. P. Perdew, M. Ernzerhof and K. Burke, *J. Chem. Phys.*, 1996, **105**, 9982.

19 G. Kresse and J. Furthmüller, *Phys. Rev. B: Condens. Matter Mater. Phys.*, 1996, **54**, 11169–11186.

20 G. Kresse and D. Joubert, *Phys. Rev. B: Condens. Matter Mater. Phys.*, 1999, **59**, 1758–1775.

21 P. E. Blöchl, *Phys. Rev. B: Condens. Matter Mater. Phys.*, 1994, **50**, 17953–17979.

22 C.-Y. Tu, A.-D. Jiang and Z.-D. Luo, *J. Struct. Chem.*, 1989, **8**, 215–219.

23 R. D. Shannon, *Acta Crystallogr.*, 1976, **A32**, 751–767.

24 M. J. Knitel, P. Dorenbos, C. W. E. van Eijk, B. Viana, A. Kahn-Harari and D. Vivien, *Nucl. Instrum. Methods Phys. Res., Sect. A*, 2000, **443**, 364–374.

25 P. Dorenbos, *Opt. Mater.*, 2017, **69**, 8–22.

26 W. J. Zhou, D. J. Hou, F. J. Pan, B. B. Zhang, P. Dorenbos, Y. Huang, Y. Tao and H. B. Liang, *J. Mater. Chem. C*, 2015, **3**, 9161–9169.

27 C. M. Liu, H. B. Liang, X. J. Kuang, J. P. Zhong, S. S. Sun and Y. Tao, *Inorg. Chem.*, 2012, **51**, 8802–8809.

28 H. H. Lin, H. B. Liang, B. Han, J. P. Zhong and Q. Su, *Phys. Rev. B: Condens. Matter Mater. Phys.*, 2007, **76**, 035117.

29 P. Dorenbos, *Phys. Rev. B: Condens. Matter Mater. Phys.*, 2001, **64**, 125117.

30 H. B. Liang, H. H. Lin, G. B. Zhang, P. Dorenbos and Q. Su, *J. Lumin.*, 2011, **131**, 194–198.

31 H. H. Lin, H. B. Liang, Z. F. Tian, Q. Su, H. Y. Xie and J. F. Ding, *J. Mater. Res.*, 2006, **21**, 864–869.

32 P. Dorenbos, *J. Lumin.*, 2013, **135**, 93–104.

33 Y. Fujimoto, T. Yanagia, Y. Yokota, N. Kawaguchi, K. Fukuda, D. Totsuka, K. Watanabe, A. Yamazaki and A. Yoshikawa, *Opt. Mater.*, 2011, **34**, 444–447.

34 P. Dorenbos, *Phys. Rev. B: Condens. Matter Mater. Phys.*, 2000, **62**, 15640–15649.

35 G. Blasse and B. C. Grabmaier, *Luminescent Materials*, Springer Verlag, Berlin, 1994.

36 P. Dorenbos, *J. Lumin.*, 2000, **91**, 155–176.

37 S. K. Pan, W. Liu, G. H. Ren, J. Y. Zhang, J. G. Pan, N. Li, Z. Wu and Y. K. Heng, *J. Alloys Compd.*, 2018, **767**, 976–981.

38 V. Jubera, J. P. Chaminade, A. Garcia, F. Guillen and C. Fouassier, *J. Lumin.*, 2003, **101**, 1–10.

39 P. Dorenbos, *ECS J. Solid State Sci. Technol.*, 2013, **2**, R3001–R3011.

40 P. Dorenbos, *J. Phys.: Condens. Matter*, 2003, **15**, 8417–8434.

41 P. Dorenbos, *J. Phys.: Condens. Matter*, 2005, **17**, 8103–8111.

42 R. F. Zhou, L. T. Lin, C. M. Liu, P. Dorenbos, Y. Tao, Y. Huang and H. B. Liang, *Dalton Trans.*, 2018, **47**, 306–313.

43 V. Bachmann, C. Ronda and A. Meijerink, *Chem. Mater.*, 2009, **21**, 2077–2084.

44 W. J. Zhou, F. J. Pan, L. Zhou, D. J. Hou, Y. Huang, Y. Tao and H. B. Liang, *Inorg. Chem.*, 2016, **55**, 10415–10424.

45 J. Ueda, P. Dorenbos, A. J. J. Bos, A. Meijerink and S. Tanabe, *J. Phys. Chem. C*, 2015, **119**, 25003–25008.

46 M. Wagner, *J. Chem. Phys.*, 1964, **41**, 3939–3943.

47 M. G. Brik, C.-G. Ma, H. B. Liang, H. Y. Ni and G. K. Liu, *J. Lumin.*, 2014, **152**, 203–205.

48 É. Tichy-Rács, Á. Péter, V. Horváth, K. Polgár, K. Lengyel and L. Kovács, *Mater. Sci. Forum*, 2013, **729**, 493–496.